Comparative evaluation of GaN transistors and Si MOSFETs for use in inductive power transfer systems of biomedical implantable devices

SOTIRIOS KOKOSIS, ELENI GATI, NIKOLAOS PATSOURAKIS and STEFANOS MANIAS
Department of Electric Power
School of Electrical & Computer Engineering
National Technical University of Athens
9 Iroon Polytexneiou St., 15780 Zografos
GREECE

Abstract: - In this work, comparative evaluation of Si MOSFETs and GaN transistors is performed for utilization in the H-bridge Voltage Source Inverter of Inductive Power Transfer Systems, developed for biomedical applications. The evaluation is made on a 10W prototype wireless charger. Simulations and experiments are carried out within two different ranges of frequencies, for a wider investigation and a more complete assessment. The efficiency results show similar performance for the two types of devices for the lower range of frequencies, whereas the superiority of GaN transistors is evident in the higher range. Ultimately, the choice of the type of semiconductor is related to the requirements of the application and the control scheme and cost are key factors that have to be taken into consideration.

Key-Words: - inductive charger, GaN, compensation, resonant circuits, implantable devices, wireless charging

1 Introduction

Inductive Power Transfer Systems (IPTSs) are used in a wide range of charging applications for electronic devices and electric vehicles, in cases where contactless power transfer is desired. Biomedical implantable devices provide a typical example of an application for which wireless power transfer is absolutely necessary. Systems providing cardiac support, like pacemakers [1], defibrillators and left ventricular assist devices (LVADs) [2],[3], are increasingly used in medicine today and new applications addressing other medical issues such as neuro-stimulators, cochlear implants [4], infusion pumps, glucose monitors etc. are gradually being developed.

These devices require electric power for their operation, which is provided by a battery implanted together with the medical device. Wireless charging of the batteries can improve the lifetime and the capabilities of such medical implants, as it eliminates the need for surgical interventions to replace empty batteries, while reducing the volume and weight of these systems, thus, allowing them to be used in even more medical applications.

IPTSs consist of a high frequency (HF) inverter, two inductively coupled coils and a rectifier, feeding the load or the battery. Power transfer is performed between the primary coil of the charger and the receiving coil, which is implanted with the medical device. The low coupling between the primary and secondary coil of such systems – coupling coefficient, *k*, commonly below 0.6 – reduces their power transfer capability. To overcome this issue compensating capacitors are incorporated, which help increase the power transfer capability of these systems by compensating for the leakage inductances, when operation at resonance is ensured. The most commonly used compensation scheme is the series-series topology, illustrated in Fig. 1, due to its high efficiency.

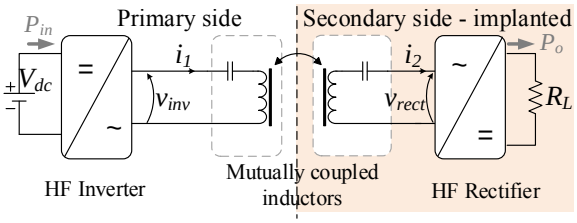

Fig. 1. Block diagram of IPTS with series-series compensation

In order to ensure a small size for the inductive charger, especially for the implanted part, the system has to operate in high frequencies. Inductive power transfer in the range of a few hundred kHz is selected over wireless charging in the MHz [5],[6] and GHz range, due to the fact that the latter is associated with a higher impact on human tissues [7],[8] compared to the former.

High frequency of operation can be efficiently supported by the new-technology semiconductors

[9],[10], and a full-bridge inverter topology is most commonly employed to allow for flexible control of the operation of the system. In order to select the type of semiconductor which is most suitable for these applications, an experimental comparison between two types of semiconductor switches is performed in this work; conventional Si MOSFETs and GaN-on-Silicon power transistors. The evaluation is carried-out on a prototype 10W IPTS designed and built for medical implant applications.

In Section 2, theoretical analysis of the series-series compensated IPTS is presented along with discussion on the most commonly selected frequencies of operation. Section 3 includes the design and experimental evaluation of the prototype magnetic link and the IPTS. Operation under both types of semiconductors is recorded and assessment of the results is performed. The main conclusions of the investigation are listed in Section 4.

2 Series-series compensated IPTS

The equivalent circuit of the series-series (SS) compensated IPTS is depicted in Fig. 2. C_1 and C_2 represent the compensating capacitors of the primary and secondary side of the system, respectively. Likewise, L_1 and L_2 are the primary and secondary coil inductances. M is the mutual inductance, $k = M/\sqrt{L_1 L_2}$, is the coupling coefficient, R_1 and R_2 are the internal resistances of the resonant circuits, R is the reflected load to the ac side of the secondary system and $v_{inv,1}$ is the first harmonic of the inverter output voltage.

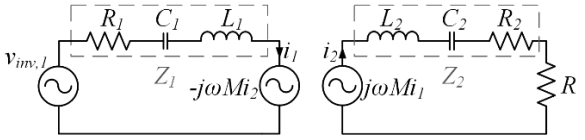

Fig. 2. First harmonic equivalent circuit of a series-series compensated Inductive Power Transfer System.

The primary and secondary side impedances, Z_1 and Z_2, are given by (1) and (2), respectively. By analyzing the equivalent circuit, the system voltage gain is calculated by (3), which results in (4).

$$Z_1 = R_1 + \frac{1}{j\omega C_1} + j\omega L_1 \tag{1}$$

$$Z_2 = R_2 + \frac{1}{j\omega C_2} + j\omega L_2 \tag{2}$$

$$\frac{v_o}{v_{inv,1}} = \frac{i_2 R}{v_{inv,1}} = \frac{j\omega MR}{(R+Z_2)\cdot Z_1 + \omega^2 M^2} \tag{3}$$

$$\frac{v_o}{v_{inv,1}} = \frac{\omega MR}{\left[\begin{array}{l}\left[(R+R_2)\left(\omega L_1 - \frac{1}{\omega C_1}\right) + R_1\left(\omega L_2 - \frac{1}{\omega C_2}\right)\right] + \\ + j\left[\left(\omega L_1 - \frac{1}{\omega C_1}\right)\left(\omega L_2 - \frac{1}{\omega C_2}\right) - R_1(R+R_2) - \omega^2 M^2\right]\end{array}\right]} \tag{4}$$

If, for simplification, the internal resistances are considered negligible, $R_1=R_2=0$, and the coupled coils are designed to be identical, $L_1=L_2=L$, and $C_1=C_2=C$ the voltage gain is provided by (5).

$$\frac{v_o}{v_{inv,1}} = \frac{\omega MR\left[R\left(\omega L - \frac{1}{\omega C}\right) - j\left[\left(\omega L - \frac{1}{\omega C}\right)^2 - \omega^2 M^2\right]\right]}{\left[R\left(\omega L - \frac{1}{\omega C}\right)\right]^2 + \left[\left(\omega L - \frac{1}{\omega C}\right)^2 - \omega^2 M^2\right]^2} \tag{5}$$

As can be seen, the output voltage depends on both the load value and the coupling coefficient of the coils.

For the selection of the frequency of operation of inductive chargers, there are three options commonly implemented in literature; the most popular, which requires no adaptation to changing conditions of the load or the coupling, is selecting a fixed frequency of operation, equal to the natural frequency of the resonant circuits, ω_n.

For operation at the natural frequency of the primary side, $\omega_n = 1/\sqrt{LC}$, the voltage gain is

$$\left|\frac{v_o}{v_{inv,1}}\right| = \frac{R\sqrt{LC}}{M} = \frac{R}{k}\sqrt{\frac{C}{L}} \tag{6}$$

Another option is the continuous adaptation of the frequency of operation of the charger to any changes in the coupling or the load. This is commonly performed in literature in two ways, both implemented with phase-locked-loop techniques, which are based on the zeroing of the phase difference between the inverter output voltage and the secondary side current (ω_r) or the primary current (ω_{PF}).

By zeroing the imaginary part of (5), the following two frequencies are obtained:

$$\omega_r = \sqrt{\frac{1}{CL(1 \mp k)}}\,. \tag{7}$$

For the above frequencies, the voltage gain is equal to 1, as explained in [11]. It is worth mentioning that using the minus (-) sign in (7), ω_r provides the frequency for which, as can be derived by (5), the output current, i_2, is in phase with the input voltage, $v_{inv,1}$. On the contrary, using the plus (+) sign results in the frequency for which the output current, i_2, has a phase difference of 180º with respect to the input voltage, $v_{inv,1}$. For the purposes of the present investigation, ω_r will, hereinafter, refer to the zero-

phase angle solution of (7), which is the frequency of interest with regard to IPTSs operation.

Unity input power factor is achieved when the inverter output voltage and the primary current are in phase. According to relations (8)-(10), the necessary condition is that $Im\{v_{inv,1}/i_1\}=0$.

$$\frac{v_{inv,1}}{i_1}=\frac{Z_1\left(R+Z_2\right)+\omega^2M^2}{\left(R+Z_2\right)} \tag{8}$$

$$Re\left\{\frac{v_{inv,1}}{i_1}\right\}=\frac{R_1\left[\left(R+R_2\right)^2+\left(\omega L_2-\frac{1}{\omega C_2}\right)^2\right]+\left(R+R_2\right)\omega^2M^2}{\left(R+R_2\right)^2+\left(\omega L_2-\frac{1}{\omega C_2}\right)^2} \tag{9}$$

$$Im\left\{\frac{v_{inv,1}}{i_1}\right\}=\frac{\left(\omega L_1-\frac{1}{\omega C_1}\right)\left[\left(R+R_2\right)^2+\left(\omega L_2-\frac{1}{\omega C_2}\right)^2\right]-\omega^2M^2\left(\omega L_2-\frac{1}{\omega C_2}\right)}{\left(R+R_2\right)^2+\left(\omega L_2-\frac{1}{\omega C_2}\right)^2} \tag{10}$$

If, for simplification, the internal resistances are considered negligible, and coupled coils are identical and $C_1=C_2=C$, (10) takes the form of (11). By setting the nominator of (11) equal to zero, unity power factor is achieved at three frequencies; the natural frequency, ω_n, ω_{PFH} and ω_{PFL}. The latter are provided by (12). At ω_n, as explained in the above, the voltage gain is given by (6), whereas, at both ω_{PFH} and ω_{PFL}, the voltage gain is dependent on both the coupling coefficient and the load value, as expressed by (13).

$$Im\left\{\frac{v_{inv,1}}{i_1}\right\}=\frac{\left(\omega L-\frac{1}{\omega C}\right)\left[R^2+\left(\omega L-\frac{1}{\omega C}\right)^2-\omega^2M^2\right]}{R^2+\left(\omega L-\frac{1}{\omega C}\right)^2} \tag{11}$$

$$\omega_{PF_L^H}=\sqrt{\frac{2L-CR^2\pm\sqrt{\left(CR^2-2L\right)^2-4\left(L^2-M^2\right)}}{2C\left(L^2-M^2\right)}} \tag{12}$$

$$\left|\frac{v_o}{v_{inv,1}}\right|=\frac{\omega_{PF_L^H}kL}{\sqrt{\left(\omega_{PF_L^H}L-\frac{1}{\omega_{PF_L^H}C}\right)^2+R^2}} \tag{13}$$

The fact that there are up to three different frequencies, including the natural frequency ω_n, for which the phase difference between i_1 and $v_{inv,1}$ is zero, is causing difficulties in the frequency tracking and control techniques employed for achieving resonance [12]. This phenomenon is known as bifurcation [13].

Due to the fact that at these frequencies the output voltage depends on the coupling coefficient and the value of the load, adoption of an output power control technique may be necessary. Using a DC/DC converter or an inverter phase-shift technique [14], [15] to properly adjust input voltage can be a suitable output power control strategy.

3 Comparative experimental evaluation

For the verification of the theoretical analysis presented in the previous Sections, simulations of the IPTS are performed for operation at the aforementioned frequencies. Additionally, a prototype inductive charger is designed and built for the experimental evaluation of the operation of the system. The respective assessment is recorded in the following subsections.

3.1 Design and evaluation of the inductive link

Most inductive chargers for biomedical implants incorporate planar circular or spiral coils [16],[3], [17], due to the space restrictions applying to the implantable coil. Optimal operation is achieved when the primary coil is perfectly aligned with the secondary coil. In such cases, the air gap ranges from 3 to 4 mm, which accounts for a typical skin depth [18].

For the evaluation of the coupling coefficient for various positions of the charger, simulations are performed with the 3D Finite Element Method software ANSYS Maxwell for the topology depicted in Fig. 3 (a). Each winding has 23 turns of litz wire, consisting of 24 strands of 0.08 mm copper wire, with a total wire diameter of 0.5 mm. The total surface diameter of each coil is 45 mm, which is within the permitted range for implants [2]. Simulations for various displacement conditions are carried out. Gap lengths in the z axis range from 3 mm to 20 mm and in the x axis from 0 mm (perfect alignment) to 15 mm. Simulations are carried out with free air as the medium.

For the experimental validation of the simulation results a prototype set of coils has been constructed, with the same specifications described in the above, as illustrated in Fig. 3 (b). The magnetic circuit is held together by a plexiglass, plastic construction (screws and nuts), which allows for relative position adjustments between the primary and secondary coils, without interfering with the magnetic flow.

The coupling coefficient for various air gaps is experimentally measured with the voltage ratio method [19]. The open-circuit voltage of each coil is measured when the other coil is excited by a high frequency alternating voltage source, V_{exc}. The excitation frequency in this case was selected at 200 kHz and the excitation source was the high-frequency

voltage source inverter, built for the inductive charger prototype. The equivalent circuit of the coupled coils is presented in Fig. 4.

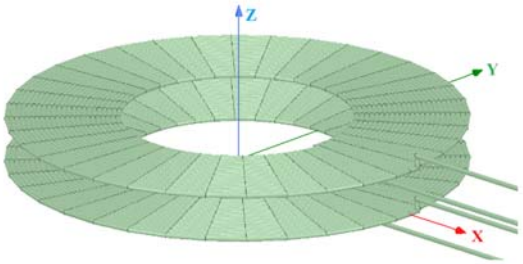

(a)

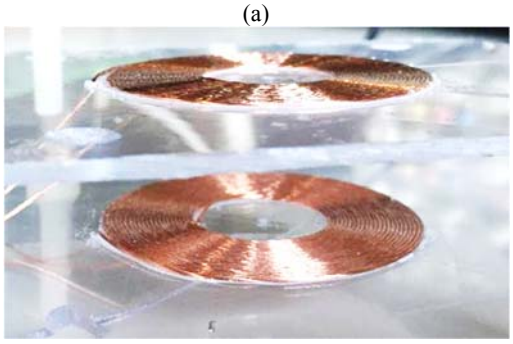

(b)

Fig. 3. (a) 3D design of primary and secondary side coils and (b) experimental setup coils.

Based on this circuit, k is obtained by the calculations provided in (14), where subscripts *1* and *2* refer to the primary and secondary coil respectively, *oc* denotes an open-circuited coil, while *exc* denotes the excited coil. L symbolizes the self-inductance and M the mutual inductance of the coils.

$$\left.\begin{aligned} V_{2oc} &= \frac{M}{L_1 - M + M}\cdot V_{1exc} \rightarrow V_{2oc} = \frac{M}{L_1}\cdot V_{1exc} \\ V_{1oc} &= \frac{M}{L_2 - M + M}\cdot V_{2exc} \rightarrow V_{1oc} = \frac{M}{L_2}\cdot V_{2exc} \end{aligned}\right\} \rightarrow$$

$$\rightarrow V_{2oc}\cdot V_{1oc} = \frac{\overbrace{M^2}^{k^2}}{L_1\cdot L_2}\cdot V_{1exc}\cdot V_{2exc} \rightarrow k = \sqrt{\frac{V_{2oc}\cdot V_{1oc}}{V_{1exc}\cdot V_{2exc}}} \quad (14)$$

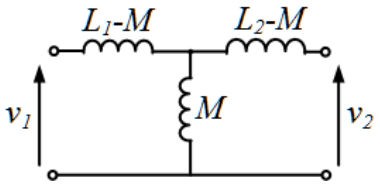

Fig. 4. Leakage equivalent circuit of inductively coupled coils.

The coupling coefficient obtained by the simulations at each position is presented in Fig. 5. As can be seen, k reaches 0.63 at the nominal position of the IPTS and may be reduced to 0.09 for the highest misaligned position tested, that is for x = 15 mm and z = 20 mm. In the same figure, the experimentally measured coupling coefficient for each position is marked by a discrete dot. The experimental results are very close to the simulation results. However, it must be noted that due to the small size of the coils, even the slightest displacement from the desired position leads to a significant change in the coupling. This factor may have contributed to the slight differentiation between the simulation and the experimental results.

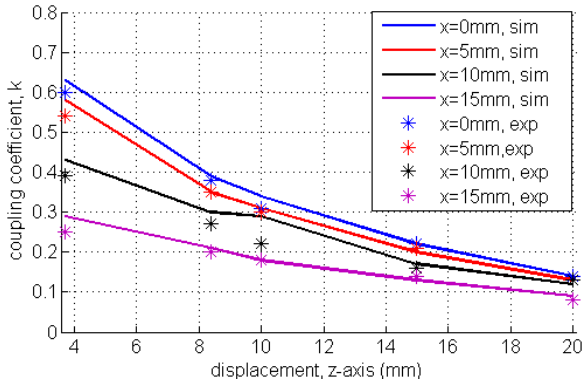

Fig. 5. Coupling coefficient, k, for various positions.

3.2 Simulations of the inductive charger

The IPTS is simulated using the Matlab/ Simulink platform, with the use of Simulink "mutual inductance" block for the inductive link and the respective power electronics blocks for the converters of the system. Namely, a full bridge inverter is used in the primary side so as to allow for controllable operation at various frequencies. A conventional full-wave rectifier is used in the secondary side of the system. The component values are presented in Table 1. A 0.5 Ω internal resistance is included in each side of the system in order to record a more realistic behavior. The inductance values have been obtained by the magnetic circuit assessment, presented in Section 3.1.

Table 1. Simulation parameters

Parameter	Value	Parameter	Value
L_1, L_2	20 μH	C_1, C_2	33 nF/4.7nF
k	0.4	R_L	20 Ω
$V_{in,DC}$	10 V	f	100-400kHz/ 400-840kHz

In order to examine the behavior of IPTSs in a wide range of frequencies, two cases of inductive systems are evaluated. The difference between the two cases is the value of the compensating capacitors, C, which is altered in order to shift the resonant frequencies to higher values. To this aim, 33 nF

capacitors are used for the first set of tested frequencies, whereas 4.7 nF capacitors are used for the second set. All the other components remain the same.

In Fig. 6 (a), the output power is recorded, for *C*= 33nF. It can be seen that for this capacitors' value the output power has a single peak and there is a single frequency at which the phase difference between the inverter output voltage and the primary current is zero (Fig. 6 (b)). The same stands, as expected for the phase difference between the inverter output voltage and the secondary current (Fig. 6 (c)).

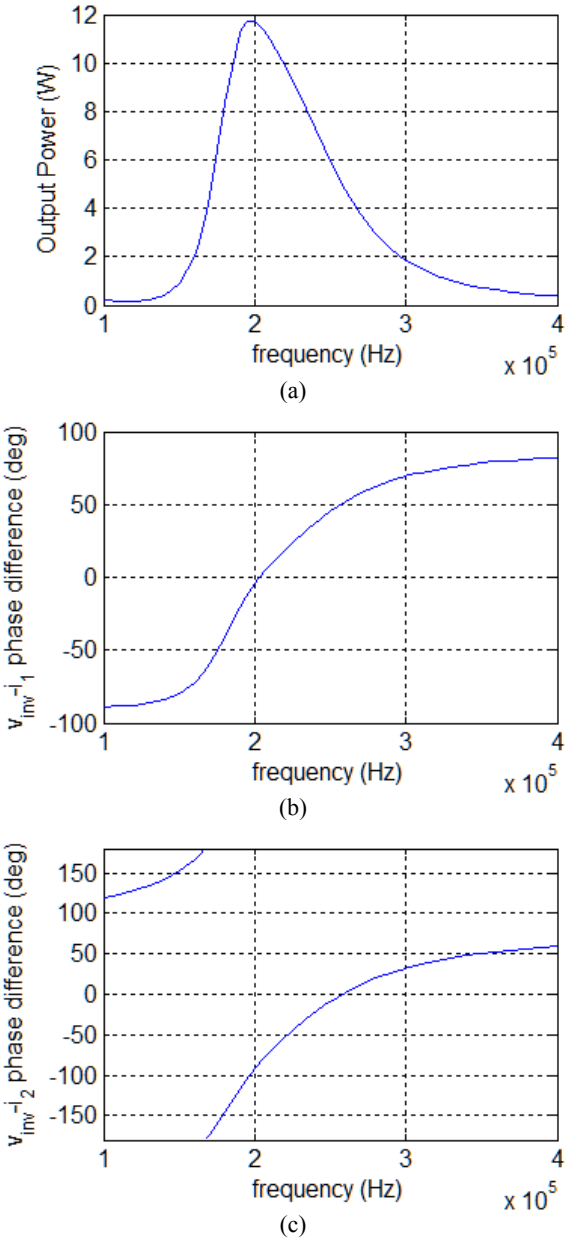

Fig. 6. (a) Output power, (b) phase difference between the inverter output voltage and the primary-side current and (c) phase difference between the inverter output voltage and the secondary-side current for C = 33 nF.

However, if the capacitors' value is switched to 4.7nF, the SS topology presents two power peaks, as shown in Fig. 7 (a), which is the result of the bifurcation phenomenon [13]. From subplot (b) of the same figure, the existence of the bifurcation phenomenon, mentioned in Section 2, is evident, since three frequencies are recorded, for which the phase difference between the inverter output voltage and the primary current is zeroed. The phase difference between the inverter output voltage and the secondary side current is also depicted in subplot (c). In the latter, one can observe the single zero-phase frequency between the inverter output voltage and the secondary current.

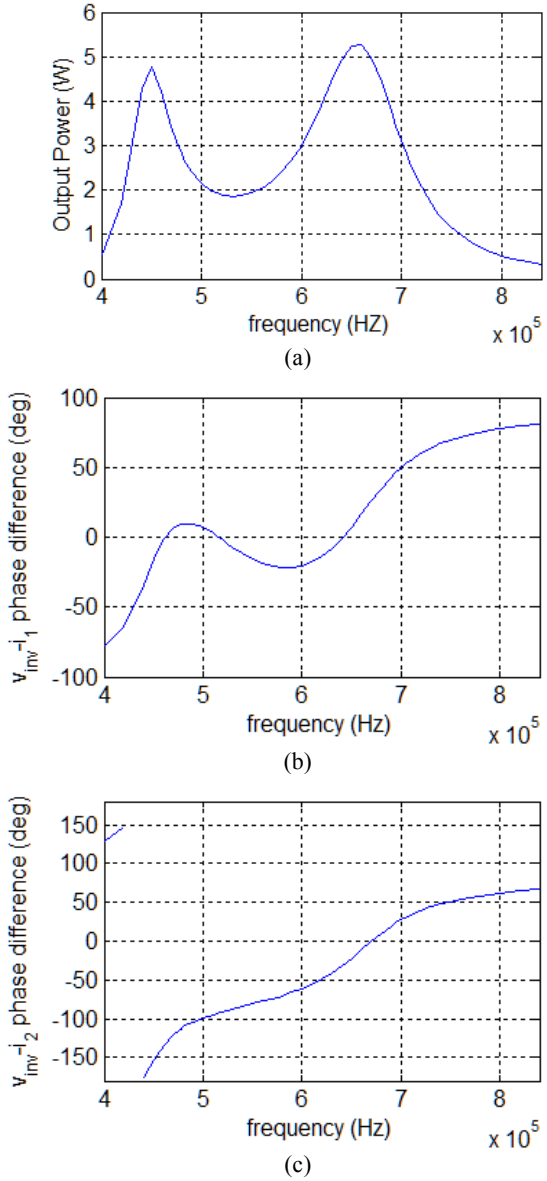

Fig. 7. (a) Output power, (b) phase difference between the inverter output voltage and the primary-side current and (c) phase difference between the inverter output voltage and the secondary-side current for C = 4.7 nF.

The complex behavior of IPTSs, as also expressed in the theoretical analysis in Section 2, can be deduced from these plots. A fully flexible and controllable excitation source is, therefore, necessary in order to allow for the implementation of sophisticated frequency and voltage control schemes. With the development of high-performance semiconductors, the full-bridge inverter topology can be taken advantage for the implementation of such systems.

3.3 Experimental comparative evaluation

The performance of the examined system is experimentally evaluated through the test-setup presented in Fig. 8. The primary side full bridge inverter was tested for comparison reasons while incorporating a) four enhancement mode GaN-on-Silicon power transistors (GS61004B) and b) four high performance Si power MOSFETs (CSD19533Q5A). The characteristics of both types of semiconductors are presented in Table 2. Both types exhibit low on-state resistance ($R_{DS\text{-}on}$) and low input charge (Q_G), favourable characteristics for high efficiency at high switching frequencies [20], with the GaN transistor being superior in all parameters but the on-state resistance.

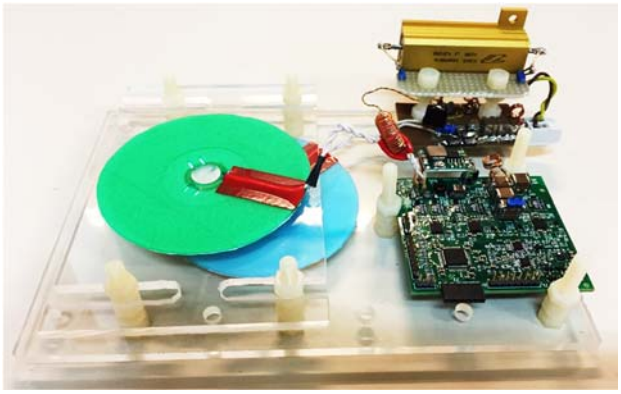

Fig. 8. Coupling coefficient, k, for various positions.

Each transistor is accompanied by an antiparallel Si Schottky barrier diode (PMEG6010) to further minimize the reverse conduction losses during the dead-time period, initially set to 30 ns. The power devices are driven by the LM5113-Q1 gate driver and 6V zener diodes are placed across the gate and source terminals to protect the devices from voltage overshoots. The secondary side rectifier consists of four Ultra -Low Forward Voltage Drop Schottky Rectifier diodes (FSV15100V) in a full bridge configuration.

The magnetic arrangement is the one presented in Section 3.1, for the evaluation of the coupling coefficient. For ease of identification and protection, the coils of Fig. 3 (b) where encapsulated in colored plexiglass pads: green for the primary and blue for the secondary side coil. The position of the coils is fixed in order to ensure same coupling conditions and, thus, fair comparison of the charger operation under the two types of semiconductors.

High-frequency current transformers were designed to accurately capture the primary and secondary side currents, while a differential probe was used to measure the primary-side voltage. The primary and secondary compensation capacitors are selected at 33nF for testing at the low range of frequencies (160 kHz - 360 kHz) and at 4.7nF for testing at the higher range of frequencies (440 kHz – 820 kHz). A 20 Ω resistive load was used for the experiments.

Table 2. Transistor characteristics

	Si (CSD19533Q5A)	**GaN (GS61004B)**
V_{DS}	100 V	100 V
Q_g	27 nC	6.2 nC
Q_{gd}	4.9 nC	0.9 nC
$R_{DS(on)}$	8.7 mΩ (@6V)	15 mΩ (@6V)
$V_{GS(th)}$	2.8 V	1.3 V
Q_{rr}	163 nC	0 nC
Cost/ piece	1.35 €	5.67 €

The recorded rise and fall times for each type of semiconductor at the higher end of each range of frequencies is depicted in Fig. 9. As expected by the characteristics of the semiconductors, the rise-time and the fall-time of the inverter output voltage when Si switches are employed is greater than the respective times of the GaN inverter.

Experiments are carried out for various frequencies within the specified ranges, in order to record the DC-DC efficiency of the system, under the use of each type of switches. Measurements are taken for a constant output power equal to 10W, which is the nominal power of the IPTS. The input voltage is appropriately adjusted in order to achieve the desired output power at each frequency of operation.

The efficiency results are presented in Fig. 10 (a) for C = 33 nF and in Fig. 10 (b) for C = 4.7 nF. From the first figure, it can be observed that the difference in the efficiency between the two types of switches is relatively small and at some frequencies non-existent, ranging from 0% to 7%.

However, the situation is different for operation at the higher range of frequencies, as illustrated in the second graph of Fig. 10. In the higher range of

frequencies, the superiority of the GaN transistors is clear and significant for most of the tested frequencies. The difference in the efficiency of the system ranges between 3% and 14%.

It is also interesting to note that the efficiency in both cases is increased for operation in the areas of the frequencies presented in Section 2, that is, around the natural frequency, ω_n, and the zero-phase frequencies, ω_r and ω_{PF}.

For a better understanding of the system operation in the above - mentioned frequencies, the experimental results are depicted in Fig. 11, at a constant output voltage of 14.14V (constant output power at 10W). From the experimental results, one can verify that, as derived by the theoretical analysis in Section 2 and the phase simulation results of sub-section 3.2, in ω_n, ω_{PFL} and ω_{PFH} the primary current is in phase with the inverter output voltage, whereas in ω_r, the secondary current is in phase with the inverter output voltage.

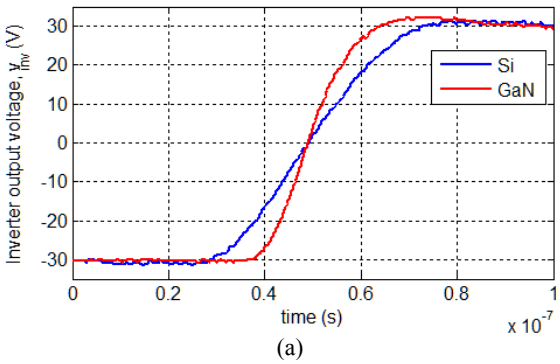

(a)

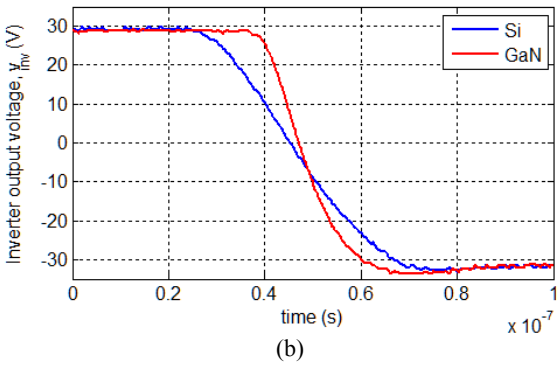

(b)

Fig. 9. Experimental results for the inverter output voltage (a) rise-time and (b) fall-time for operation at 360 kHz, C=33nF.

4 Conclusion

In this work, comparative evaluation of the use of Si MOSFETs and GaN transistors is performed in an inductive charger for medical implantable devices. Theoretical analysis of the series-series compensated IPTS has highlighted the complexity of the operation of such systems and has provided the most preferable frequencies of operation. Simulations and experimental results have verified the theoretical analysis.

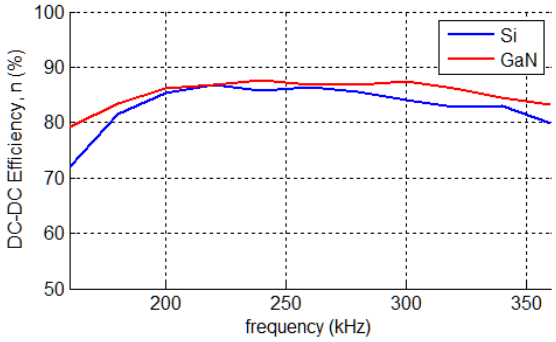

(a)

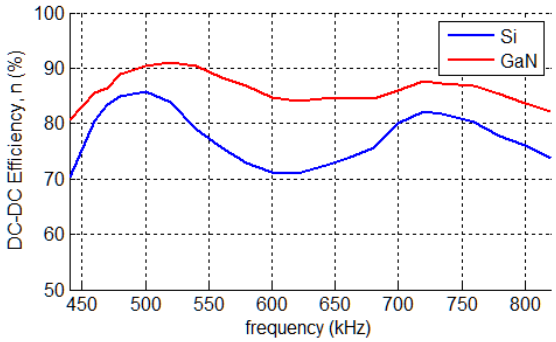

(b)

Fig. 10. DC-DC efficiency for (a) C = 33nF and (b) C = 4.7nF.

Regarding the effect of the type of semiconductor used in the efficiency of the system, the experimental results for the 160 - 360 kHz range of frequencies have shown insignificant differences, especially for operation close to the frequencies obtained by the theoretical analysis. Due to the very small difference in the efficiency and the fact that the current cost of GaN semiconductors is more than 4 times higher than that of the respective Si MOSFETs, selection of the latter is suggested. On the contrary, the experimental results for the 440 - 820 kHz range of frequencies highlight the superiority of GaN transistors and, in this case, their use over their Si counterparts is recommended, despite the additional cost.

It is worth mentioning that there are biomedical devices, like cochlear implants, for which the patient is constantly carrying both the primary system (attached but not implanted) and the secondary system (implanted), and the primary is wirelessly feeding the secondary system with the use of an external battery. In these types of biomedical applications the system efficiency is of great importance, since the attached primary has to incorporate a very small sized battery and it is more convenient for the patient if the recharging of this battery is infrequent. Therefore, in such cases, the use

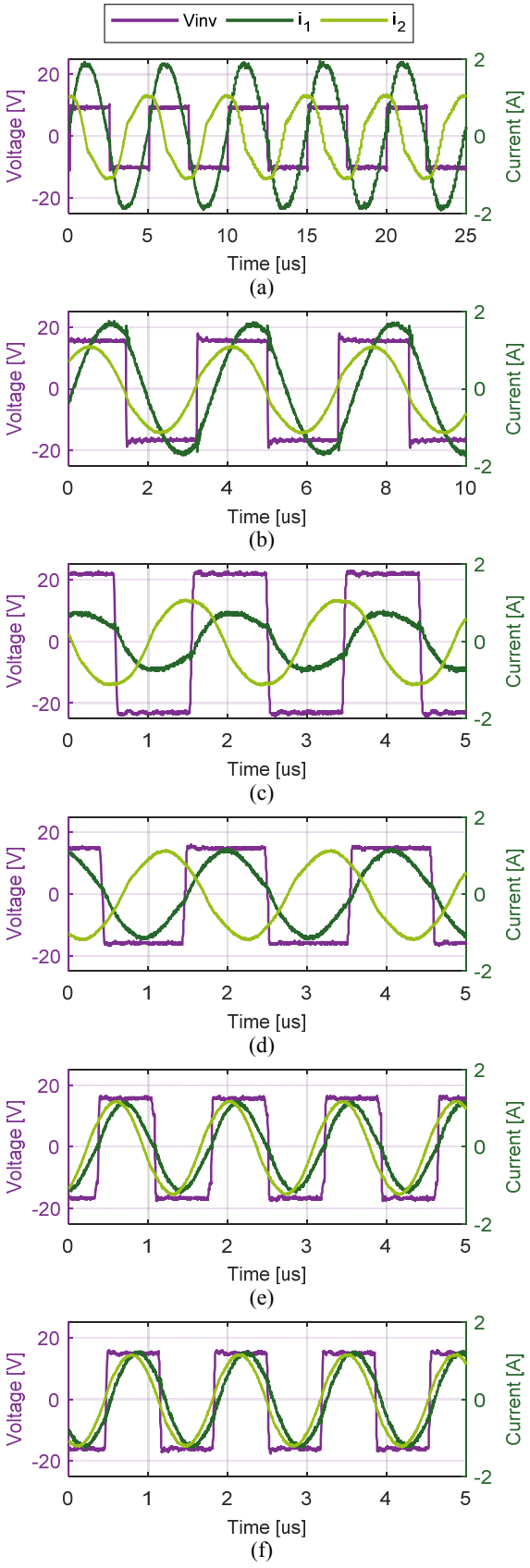

Fig. 11. Experimental results for C=33nF (a) at ω_n=200kHz, (b) at ω_r = 280kHz and for C=4.7nF (c) at ω_n = 520kHz, (d) at ω_{PFL}=480kHz, (e) at ω_{PFH}=700khz and (f) at ω_r=735kHz

of GaN transistors is unquestionably the best option, since achieving the highest possible efficiency is a more important than reducing the system cost. In other applications, for which efficiency is not a key factor, the newest technology Si MOSFETs can be a good option for inductive power transfer at lower frequencies.

5 Acknowledgement

This research is carried out in the context of the project "*Advanced wireless charging techniques for medical implant applications*" (MIS 5004934) under the call for proposals "*Supporting Researchers with an Emphasis on Young Researchers*" (EDULLL 34). The project is co-financed by Greece and the European Union (European Social Fund- ESF) by the Operational Programme Human Resources Development, Education and Lifelong Learning 2014-2020.

Ευρωπαϊκή Ένωση
European Social Fund

Operational Programme
Human Resources Development,
Education and Lifelong Learning
Co-financed by Greece and the European Union

ΕΣΠΑ
2014-2020

References:

[1] T. Campi, S. Cruciani, F. Palandrani, V. De Santis, A. Hirata, and M. Feliziani, "Wireless Power Transfer Charging System for AIMDs and Pacemakers," *IEEE Trans. Microw. Theory Tech.*, vol. 64, no. 2, pp. 633–642, Feb. 2016.

[2] O. Knecht, R. Bosshard, and J. W. Kolar, "High-Efficiency Transcutaneous Energy Transfer for Implantable Mechanical Heart Support Systems," *IEEE Trans. Power Electron.*, vol. 30, no. 11, pp. 6221–6236, Nov. 2015.

[3] O. Knecht and J. W. Kolar, "Performance Evaluation of Series-Compensated IPT Systems for Transcutaneous Energy Transfer," *IEEE Trans. Power Electron.*, vol. 34, no. 1, pp. 438–451, Jan. 2019.

[4] V. Nair and J. Choi, "An Integrated Chip High-Voltage Power Receiver for Wireless Biomedical Implants," *Energies*, vol. 8, no. 6, pp. 5467–5487, Jun. 2015.

[5] S. Zhong, C. Yao, H.-J. Tang, and K.-X. Ma, "Research and Design of Coupled Magnetic Resonant Power Transfer System," *WSEAS Trans. CIRCUITS Syst.*, vol. 14, pp. 253–261, 2015.

[6] N. Jamal, S. Saat, and Y. Yusmarnita, "A Development of Class E Converter Circuit for Loosely Coupled Inductive Power Transfer System," *WSEAS Trans. Circuits Syst.*, vol. 13, no. 1, pp. 1–4, 2014.

[7] J. S. Ho, S. Kim, and A. S. Y. Poon, "Midfield

Wireless Powering for Implantable Systems," *Proc. IEEE*, vol. 101, no. 6, pp. 1369–1378, Jun. 2013.

[8] S. Bakogianni and S. Koulouridis, "Sub-1 GHz far-field powering of implantable medical devices: Design and safety considerations," in *2015 IEEE International Symposium on Antennas and Propagation & USNC/URSI National Radio Science Meeting*, 2015, vol. 2015-Octob, pp. 942–943.

[9] K. J. Chen *et al.*, "GaN-on-Si Power Technology: Devices and Applications," *IEEE Trans. Electron Devices*, vol. 64, no. 3, pp. 779–795, Mar. 2017.

[10] O. C. Spro, O.-M. Midtgrd, T. Undeland, and G. Guidi, "Development of a full bridge GaN HEMT converter for inductive power transfer application," in *2016 IEEE 4th Workshop on Wide Bandgap Power Devices and Applications (WiPDA)*, 2016, pp. 30–34.

[11] E. Gati, G. Kampitsis, and S. Manias, "Variable Frequency Controller for Inductive Power Transfer in Dynamic Conditions," *IEEE Trans. Power Electron.*, vol. 32, no. 2, pp. 1684–1696, Feb. 2017.

[12] J. T. Boys, G. a. Covic, and A. W. Green, "Stability and control of inductively coupled power transfer systems," *IEE Proc. - Electr. Power Appl.*, vol. 147, no. 1, p. 37, 2000.

[13] C.-S. Wang, G. A. Covic, and O. H. Stielau, "Power Transfer Capability and Bifurcation Phenomena of Loosely Coupled Inductive Power Transfer Systems," *IEEE Trans. Ind. Electron.*, vol. 51, no. 1, pp. 148–157, Feb. 2004.

[14] K. Song, Z. Li, Z. Du, G. Wei, and C. Zhu, "Design for constant output voltage and current controllability of primary side controlled wireless power transfer system," in *2017 IEEE PELS Workshop on Emerging Technologies: Wireless Power Transfer (WoW)*, 2017, pp. 1–6.

[15] S. Manias, *Power Electronics and Motor Drive Systems*. Academic Press, Elsevier Inc., 2017.

[16] H. Mo and H. Tang, "A Magnetic Resonant Coupling Printed Spiral Coil System under Different Geometric Values," *WSEAS Trans. Circuits Syst.*, vol. 14, pp. 442–447, 2015.

[17] A. K. RamRakhyani, S. Mirabbasi, and M. Chiao, "Design and Optimization of Resonance-Based Efficient Wireless Power Delivery Systems for Biomedical Implants," *IEEE Trans. Biomed. Circuits Syst.*, vol. 5, no. 1, pp. 48–63, Feb. 2011.

[18] D. P. Chandima, K. D. U. . Dayarathna, H. G. D. . Jayasinghe, W. K. K. . Dharmasiri, and H. . Weerasinghe, "Inductive power transmission, charging and communication for implantable devices," in *2017 IEEE International Conference on Industrial and Information Systems (ICIIS)*, 2017, pp. 1–6.

[19] E. Gati, A. Kladas, and S. Manias, *Examination of a split transformer arrangement for the inductive link of contactless power transfer systems*, vol. 856. 2016.

[20] A. Nakajima, M. Shimizu, and H. Ohashi, "Power Loss Limit in Unipolar Switching Devices: Comparison Between Si Superjunction Devices and Wide-Bandgap Devices," *IEEE Trans. Electron Devices*, vol. 56, no. 11, pp. 2652–2656, Nov. 2009.